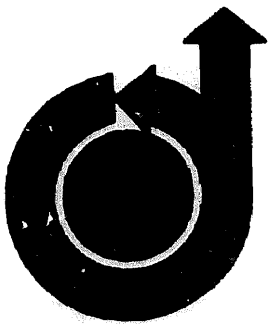

AIAA Paper
No. 70-90

SUPERSONIC MIXING OF TWO-PHASE CO-FLOWING JETS

by
CLAYTON LaPOINTE
University of Michigan
Ann Arbor, Michigan

AIAA 8th Aerospace Sciences Meeting

NEW YORK, NEW YORK/JANUARY 19-21, 1970

SUPERSONIC MIXING OF TWO-PHASE CO-FLOWING JETS

Clayton LaPointe*
Gas Dynamics Laboratories
The University of Michigan
Ann Arbor, Michigan

Abstract

Experimental results pertaining to Mach 3 axisymmetric mixing of water droplets and air are presented. The droplets exhibit monodisperse light scattering characteristics. The mean droplet diameter, determined from transverse transmission measurements at two infrared wave lengths, is 7.35 ± 0.10 microns throughout the jet. This agrees with extrapolated subsonic data. Path-integrated transmission measurements are point-resolved via numerical Abel transformation. Particle number density profiles are obtained as a function of the jet's radial and axial coordinates. Two regions, corresponding to the outer jet's potential core and eventual fully-developed region, are considered In the potential region, the droplet density radial profile is gaussian and the centerline value decays as $z^{-5/3}$. A linear jet spreading rate is noted. In the fully-developed region, the wings of the density profile lie above the gaussian curve and the centerline density decays as $z^{-7/3}$. The jet spreading rate in the latter region varies as $z^{-5/3}$. Centerline density and spreading rates are obtainable by graphical techniques without resort to complete Abel inversion of the transverse data..

I. Introduction

The mixing of gaseous fuel with a supersonic air stream has been studied by a number of authors[1, 2, 3]. Their efforts have been largely directed toward obtaining expressions for turbulent transport coefficients in terms of gross flow variables and determining the regions of applicability of similarity solutions. Requisite to the construction of such solutions are analytic expressions for the spatial behavior of centerline concentration, spreading rate, and velocity. Power-law dependences upon axial distance have been found experimentally by means of direct physical probes.

In situations where liquid fuel mixes with supersonic air, direct probing is difficult to apply. Another variable, the fuel droplet size distribution, plays an important role. As the mean droplet size decreases and the velocity increases, the usual photographic particle size determination techniques become less practical. On the basis of subsonic data[4] extrapolated to a Mach 3 mixing situation, the mean particle size should be of the order of a few microns (Figure 1). In addition, Figure 2 shows that the particle size distribution at high relative velocity is extremely narrow. Thus, the particles produced by high aerodynamic shear should all be approximately the same size. Regarding their light scattering behavior, this situation is termed monodisperse and constitutes a much simpler case to interpret than does the more general polydisperse situation. Dobbins[5] has studied, by light scattering techniques, the size distribution of polydisperse Al_2O_3 particles formed in solid propellant rocket chambers. He concludes[6] that more than one particle generation mechanism, leading to a double-humped size distribution function, must be postulated to reconcile his data with that of Crowe and Willoughby[7] who used tank collection techniques. The resulting distribution function, a combination of an Upper Limit Distribution Function (ULDF)[8] with a delta function, requires five parameters for its specification which, in principle, must be determined by five independent experimental measurements. A sixth measurement is required to determine the particle number density.

If, however, the particle size distribution may be approximated by a delta function, then only two independent measurements are required to determine the mean particle size and number density. Unfortunately, one usually does not know the nature of the particle size distribution function beforehand, It turns out, however, that a monodisperse scattering situation may be experimentally verified through a suitable choice of probe wavelengths. This paper reports the results of such a light scattering experiment applied to Mach 3 coaxial mixing of water particles and air. Two wavelengths in the near infrared are employed to map the particle size, number density and mean velocity distribution. As in the subsonic case, power-law behavior of several jet descriptors is noted The radial distribution of number density is obtained by means of Abel inversion,

II. ical ormulation

The measurement involves recording the transmission loss suffered by a beam of light as it traverses a cylindrical stream of water droplets. (Figure 3). The light beam lies in a plane perpendicular to the axis of symmetry and that portion within the jet descr[illegible] the chord of a circle.

*Presently with Scientific Research Staff, Ford Motor Company, Dearborn, Michigan 48121

It has been shown[9] that forward scattering may be neglected provided the solid angle subtended by the collector optics is sufficiently small. The length of the optical path within the jet is L, a function of the transverse coordinate, y. It is customary to define the sense of the path variable, ℓ, such that $\ell = 0$ at the boundary nearest the observer and increases positively into the scattering medium. Thus light enters the jet at $\ell = L(y)$ and emerges at $\ell = 0$. In these coordinates, the differential attenuation suffered by the beam while traversing a length, $d\ell$, is given by[10]

$$\frac{dI_\lambda}{d\ell} = K_\lambda I_\lambda \tag{1}$$

where I_λ = spectral radiance
K_λ = scattering extinction coefficient

The extinction coefficient is proportional to the number of particles and their cross-section within the scattering volume. The efficiency with which a single particle scatters radiation is described by the scattering area coefficient, K_s. For a polydispersion whose particle size distribution function is $\phi(D)$, the extinction coefficient is given by[11]

$$K_\lambda = \frac{\pi}{4} N \int_0^\infty K_s\left(\frac{\pi D}{\lambda}\right) \phi(D)\, D^2 dD \tag{2}$$

where N = particle density
D = particle diameter
λ = wavelength
and $\phi(D)$ is normalized such that $\int_0^\infty \phi(D) dD = 1$.

An observer measuring $I_\lambda(y,z)$ emerging from the near jet boundary sees only the cumulative effect of the non-homogeneous scattering between $\ell = 0$ and $\ell = L$. If the incident radiation is denoted by I_λ^0, then the fraction transmitted is given by

$$-\ln \frac{I_\lambda(y,z)}{I_\lambda^0} = \int_0^{L(y,z)} K_\lambda(r,z)\, d\ell \tag{3}$$

Let a_λ be the fraction of I_λ^0 lost by scattering. Then transforming to cylindrical coordinates, Eq. (3) becomes

$$-\ln\left[1 - a_\lambda(y,z)\right] = 2 \int_y^{R(z)} K_\lambda(r,z) \frac{r\, dr}{(r^2 - y^2)^{1/2}} \tag{4}$$

where R is the jet radius. This is an Abel integral equation, the inverse of which is[12]

$$K_\lambda(r,z) = \frac{1}{\pi} \int_r^{R(z)} \frac{d}{dy} \ln[1 - a_\lambda(y,z)] \frac{dy}{(y^2 - r^2)^{1/2}} \tag{5}$$

Thus the Cartesian mapping, $a_\lambda(y,z)$, is converted to the polar mapping, $K_\lambda(r,z)$. Any of a number of published[13] Abel inversion techniques may be employed.

Relating $K_\lambda(r,z)$ to the number density and particle size is accomplished by taking transverse a_λ measurements at two wavelengths. The process is described below.

In axisymmetric flow, the water mass flow rate is given by

$$\dot{m}_w = 2\pi \int_0^R \rho\, u\, r\, dr \tag{6}$$

where ρ = water mass density

$$= \frac{\pi}{6} \rho_w N \int_0^\infty \phi(D) D^3 dD \tag{7}$$

u = velocity
ρ_w = liquid density

Introducing the scattering parameter, $\alpha = \pi D/\lambda$ and defining the average velocity,

$$\langle u \rangle = \frac{\int_0^R \frac{\overline{\alpha^3}}{\alpha^3} N u r\, dr}{\int_0^R \overline{\alpha^3} N r\, dr} \tag{8}$$

leads to

$$\dot{m}_w = \frac{\lambda^3}{3\pi} \rho_w \langle u \rangle \int_0^R \overline{\alpha^3} N r\, dr \tag{9}$$

where $\overline{a^3}$ is the third moment of the particle size distribution, i.e.:

$$\overline{\alpha^n} = \int_0^\infty \alpha^n \phi(\alpha)\, d\alpha \tag{10}$$

Further defining

$$\alpha_{32} = \frac{\overline{\alpha^3}}{\overline{\alpha^2}} \tag{11}$$

the mean particle volume to mean area ratio, and substituting for N from Eq. (2) yields

$$\dot{m}_w = \frac{4}{3}\rho_w \lambda \langle u \rangle \int_0^R \frac{\alpha_{32}}{\bar{\bar{K}}_s} K_\lambda \, r \, dr \tag{12}$$

where

$$\bar{\bar{K}}_s = \overline{K_s \alpha^2} / \overline{\alpha^2} \tag{13}$$

is the area-weighted average scattering coefficient. The ratio, $\bar{\bar{K}}_s/\alpha_{32}$, has been termed the specific scattering area coefficient[11].

Proceeding formally, one further average is defined as

$$\left\langle \frac{\alpha_{32}}{\bar{\bar{K}}_s} \right\rangle = \frac{\int_0^R \frac{\alpha_{32}}{\bar{\bar{K}}_s} K_\lambda \, r \, dr}{\int_0^R K_\lambda \, r \, dr} \tag{14}$$

Such that $\dot{m}_w$ may finally be expressed,

$$\dot{m}_w = \frac{4}{3}\rho_w \lambda \langle u \rangle \left\langle \frac{\alpha_{32}}{\bar{\bar{K}}_s} \right\rangle \int_0^R K_\lambda \, r \, dr \tag{15}$$

Since no water is entrained from the atmosphere, m_w is a conserved quantity with respect to jet axial distance, z. Further, $K_\lambda(r,z)$ is a measurable quantity. Therefore the integral in Eq. (15) may be determined by integration of the Abel-inverted data or by taking advantage of a property of the Abel transformation to obtain it directly, This wilt be discussed later.

If experiments are performed at two separate wavelengths with the same jet flow conditions, the following ratio may be formed from Eq. (15)

$$\frac{\left\langle \frac{\alpha_{32}}{\bar{\bar{K}}_s} \right\rangle_{\lambda_1}}{\left\langle \frac{\alpha_{32}}{\bar{\bar{K}}_s} \right\rangle_{\lambda_2}} = \frac{\lambda_2}{\lambda_1} \frac{\int_0^R K_{\lambda_2} \, r \, dr}{\int_0^R K_{\lambda_1} \, r \, dr} \tag{16}$$

The right hand side of this equation is measured. The left hand side depends only on $\phi(\alpha)$ for a particular scattering fluid. As it stands, the equation applies to a polydisperse medium whose $\phi(\alpha)$ may also depend on r and z. If the particle size, α_{32}, is a slowly varying function of the radial coordinate compared to N(r), then the average, Eq. (14), may be replaced by $\alpha_{32}/\bar{\bar{K}}_s$ evaluated at some intermediate radius, r', determined by the weighting function, $K_\lambda r$. In this case, Eq. (16) becomes

$$\left.\frac{\frac{\bar{\bar{K}}_s(r')}{\alpha_{32}(r')}}{\frac{\bar{\bar{K}}_s(r')}{\alpha_{32}(r')}}\right|_{\lambda_2} = \frac{\lambda_2}{\lambda_1} \frac{\int_0^R K_{\lambda_2} \, r \, dr}{\int_0^R K_{\lambda_1} \, r \, dr} \tag{17}$$

The data analysis procedure is as follows A plot (Fig. 4) of $\bar{\bar{K}}_s/\alpha_{32}$ versus α_{32}, for various $\phi(\alpha)$, is constructed on log-log paps–. The wavelengths are chosen such that both α_{32}'s will lie in the region of most rapid $\bar{\bar{K}}_s/\alpha_{32}$ variation. This is estimated by extrapolating subsonic data or by actually performing two measurements and checking the slopes obtained. Since D_{32} is the same for both wavelengths, $\alpha_{32}(\lambda_1)$ will be related to $\alpha_{32}(\lambda_2)$ by the ratio λ_2/λ_1. Choose $\lambda_2 > \lambda_1$ such that $\alpha_{32}(\lambda_1)/\alpha_{32}(\lambda_2)$ is greater than one. On log-log paper, the abscissa1 separation of the two solutions is of length $\log \lambda_2/\lambda_1$. Similarly, the ordinal separation of $(\bar{\bar{K}}_s/\alpha_{32})_{\lambda_1}$ and $(\bar{\bar{K}}_s/\alpha_{32})_{\lambda_2}$ is of length (Eq. (17)).

$$\log \frac{\lambda_1 \int_0^R K_{\lambda_1} \, r \, dr}{\lambda_2 \int_0^R K_{\lambda_2} \, r \, dr}$$

An overlay, with the measured ordinal and abscissal lengths forming the legs of a right triangle, may now be employed to search the $\bar{\bar{K}}_s/\alpha_{32}$ curve for simultaneous solution points. Once $\alpha_{32} = (\pi/\lambda) D_{32}$ is determined, the particle density may be obtained from Eq. (2) in the averaged form,

$$K_\lambda = \frac{\lambda^2}{4\pi} \bar{\bar{K}}_s \overline{\alpha^2} N \tag{18}$$

Finally, the average velocity may be obtained from Eq. (15).

In principle, it is possible to unambiguously determine which $\phi(\alpha)$ yields the correct $\bar{\bar{K}}_s$ curve by repeated application of the above procedure using several wavelengths. It has been shown[11]

that the actual shape of $\phi(\alpha)$, provided it is single-humped, is of minor significance in determining the various averages over the particle distribution. The major influencing factor is the width of $\phi(\alpha)$. For this reason, the $\tilde{K}_s/\alpha_{32}$ curves of Fig. 4 have been computed assuming a top-hat distribution whose relative widths, $\Delta\alpha/\alpha_{32}$, vary from 0 (delta function) to ∞. In computing these curves, the scattering area coefficient for a single water particle in air was obtained from the Mie scattering theory as reported by Houghton and Chalker[10].

A number of simplifications of the data reduction procedure are possible. Without loss of generality, many variables of interest, including the centerline number density, may be obtained without Abel inversion.

The cross-sectional integral of K_λ is required in the solution of Eq. (17). Since $K_\lambda(r)$ must first be determined by Abel inversion of $a_\lambda(y)$, this integral constitutes an additional operation on the reduced data. These two operations may be circumvented by the relation[12]

$$\pi \int_0^R K_\lambda(r)\, r\, dr = -\int_0^R \ln\left[1 - a_\lambda(y)\right] dy \qquad (19)$$

which states that the area under the transverse data is equal to the cross-sectional integral of the physical, quantity sought. This relation is often used to check Abel transforms. Whereas $-\ln[1 - a_\lambda(y)]$ is one of the transform pairs, what is initially measured is $a_\lambda(y)$ itself. Due to the occurrence of the natural logarithm in the above integrand, the integral may be partially integrated to yield

$$\int_0^R K_\lambda(r)\, r\, dr = \frac{1}{\pi} \int_0^{a_\lambda(0)} \frac{y}{1 - a_\lambda}\, da_\lambda \qquad (20)$$

where $a_\lambda(0)$ is the centerline value of $a_\lambda(y)$. In no instance was complete attenuation ever measured so that the denominator of the integrand was never zero. The integral in question is depicted by the shaded area of Fig. 5.

The centerline value of K_λ may be determined from Eq. (5) by setting the lower limit of integration equal to zero. As in the previous case, the resulting integral may be partially integrated.

$$K_\lambda(0, z) = \frac{1}{\pi} \int_0^{a_\lambda(0)} \frac{da_\lambda}{y\,(1 - a_\lambda)} \qquad (21)$$

The denominator in this case does go to zero within the range of integration but the integral is, of course, convergent since K_λ is everywhere finite. In practice, the area under the divergent portion of the integrand contributes relatively little to the integral as shown in Fig. 6. The centerline variation of K_λ turns out to be due almost entirely to variation in number density for the experimental conditions investigated.

Two measures of the jet spreading rate may also be obtained without Abel transformation. In experiments utilizing physical probes, the most common measure of jet spread is the half-radius, $r_{1/2}$, of either velocity or injected fluid density. This radius may be obtained using the present line probe technique only after performing an Abel inversion. Advantage may be taken of the integral nature of the scattering technique to define two additional characteristic radii, r_1 and r_2, which, for flows exhibiting similarity radial profile behavior, are proportional to $r_{1/2}$. These characteristic radii are:

$$r_1(z) = \frac{\int_0^R K_\lambda(r)\, r\, dr}{\int_0^R K_\lambda(r)\, dr} = \frac{2\int_0^{a_\lambda(0)} \frac{y}{1 - a_\lambda}\, da_\lambda}{-\pi \ln\left[1 - a_\lambda(0)\right]} \qquad (22)$$

and

$$r_2(z) = \frac{\int_0^R K_\lambda(r)\, dr}{K_\lambda(0)} = \frac{-\pi \ln\left[1 - a_\lambda(0)\right]}{2\int_0^{a_\lambda(0)} \frac{da_\lambda}{y(1 - a_\lambda)}} \qquad (23)$$

where use has been made of Eq. (4), (20), and (21). The utility of defining these integral radii stems from the present method of measurement which is basically integral in nature. These radii are therefore easy to measure. They also have the advantage, since they do involve integration, of being less susceptible to noise interference than point measurements. The physical significance of r_1 and r_2, as well as $\langle u \rangle$ may be seen by recasting Eq. (12) in the form

$$\dot{m}_w = \frac{4}{3} \rho_w A \langle u \rangle \left\langle \frac{\alpha_{32}}{K_s} \right\rangle \pi r_1 r_2 K_\lambda(0) \qquad (24)$$

and comparing to the one-dimensional continuity equation, $\dot{m} = \rho A V$. The following identifications may be made:

1. Effective cross-sectional area

$$A = 2\pi r_1 r_2$$

2. Mass density

$$\rho = \frac{3}{4} \rho_w \lambda \left\langle \frac{\alpha_{32}}{K_s} \right\rangle K_\lambda(0)$$

3. Average cross-sectional velocity

$$V = \langle u \rangle$$

III. Experiment Description

The light scattering technique developed above has been applied to supersonic coaxial mixing of water centrally injected into a free air jet (Fig. 7). Nozzle and injector operating parameters are summarized in Table 1.

Nozzle exit diameter	1.786 cm
Injector diameter	0.475 cm
Jet exit area	2.33 cm^2
Exit Mach No. (air)	3.0
Exit velocity (air)	6×10^4 cm/sec
Stagnation temperature	300°K
Exit air density	3.6×10^{-3} gm/cm^3
Air mass flow rate	500 gm/sec
Water mass flow rate	7.4 gm/sec
Exit Reynolds No.	2.4×10^6
Mass flux ratio (W/A)	0.44

Table 1. Nozzle Operating Parameters

The mixing jets exhausted vertically through a hole in the optical platform (Fig. 8). Transverse scanning of the jet was accomplished by horizontal translation of the optical platform and axial scanning by vertical translation of the jet itself. All optical components were shock mounted.

A chopper-modulated tungsten filament is brought to a focus at the central plane of the jets and again at the entrance slit of a Perkin-Elmer Model 98-G monochromator. The f/12 optical system is entirely reflective and arranged antisymmetrically to minimize aberrations. The entrance slit, which defines spatial resolution, is aligned in the direction of the flow. A slit of width 100 μm and a height of 1.2 cm was used.

In operation, the monochromator was set to a wavelength in the near infrared region. Care was taken to avoid water absorption bands. The beam attenuation due to scattering was then monitored by a lead sulphide cell whose output was synchronously detected by a PAR Model 120 lock-in amplifier. The amplifier output was displayed on an x-y recorder whose abscissa was driven by a linear potentiometer attached to the optical platform. In this way, $a_\lambda(y)$ was obtained.

The results of this experiment, for one fuel/air ratio and several axial locations, are presented below.

IV. Results

The specific scattering-area coefficient, $\bar{K}_s/\alpha_{32}$, and the mean particle size, D_{32}, have been determined by the ratio technique of Section II. It was found that only the monodisperse curve of $\bar{K}_s/\alpha_{32}$ provided consistent solutions. When it is recalled that particles of differing sizes anywhere in the optical path will tend to smooth $\langle \bar{K}_s/\alpha_{32} \rangle$, it must therefore be concluded that the particles generated in the vicinity of the injector exit are all of the same approximate diameter ana remain so as they diffuse downstream. In this situation, $\langle \bar{K}_s/\alpha_{32} \rangle \rightarrow K_s/\bar{\alpha}$ and monodisperse analysis may be applied throughout the data reduction process. As mentioned in the Introduction, this result was not unexpected. The particle size is 7.35 ± 0.10 μm throughout the measured portion of the jet (9-46 nozzle radii).

The *axial* variations of the extinction coefficient (centerline value, path-integral and jet cross-sectional area integral) for two wavelengths are shown in Fig. 9. Two features are immediately apparent concerning these data: there is a quantitative difference between corresponding magnitudes measured at the two wavelengths, $\lambda_1 = 1.6$ μm and $\lambda_2 = 2.38$ μm and the shorter wavelength data is consistently higher in magnitude than the longer wavelength data. This indicates that the wavelengths chosen are in the desired region of the $\bar{K}_s/\alpha_{32}$ curve. Were the wavelengths much shorter, the quantitative behavior would be reversed (Rayleigh scattering region); were they much longer, no quantitative difference would be noticed (geometrical optics limit).

The slopes of the data indicate power-law behavior over much of the measured jet length. This behavior is evidenced in two separate regions corresponding to the initial and fully-developed regions of Fig. 7. Power-law behavior is, of course, important in formulating similarity solutions.

Without further reduction, the integral radii, r_1 and r_2 may be obtained directly from the data of Fig. 9. In view of the constancy of D, these radii (Fig. 10) are indicative of the particle density profiles, N(r). As in subsonic flow, both radii initially increase linearly but then, due to rapid turbulent diffusion, spread as the 5/3 power

of axial distance. The nature of their definition requires they be proportional to each other provided the N(r) profiles exhibit similarity behavior with respect to axial distance. This proportionality is evident in the figure for $z/r_0 < 20$ and again for $z/r_0 > 30$. If the N(r) profile is gaussian, then $r_2 = 1.59\ r_1$. This is indeed the ratio measured in the initial region and is confirmed by actual Abel inversion.

The centerline particle density is shown in Fig. 11. This is an important determination and is the subject of some controversy in the literature. Direct probe measurements of subsonic, incompressible, mixing of two gases indicate a z^{-1} dependence for N(0). One investigator[2] has measured a z^{-2} dependence of N(0) for supersonic mixing of H_2 with air. Schetz[1] has pointed out an apparent mass flux ratio dependence for this exponent of z. For $\rho u_w/\rho u_a < 1$, the centerline concentration as measured by several investigators and reported by Schetz varies roughly as $z^{-2 \pm 0.4}$. For $\rho u_w/\rho u_a > 1$, this exponent changes abruptly to -1. (The subscripts, w and a, here refer to any injected gas and surrounding medium respectively.) The present data is consistent insofar as $\rho u_w/\rho u_a$ is < 1 and the decay exponent of z is near -2. It is possible to go further than this in discussing the present data, however.

Since overlapping data have been obtained by the present methods, there are consistency checks in the data reduction process. Where data concerning, say, r_2 may exhibit some scatter, there is data concerning r_1 which may not. This self-checking procedure has been employed with the result that it is certain that N(0) exhibits a change in decay exponent in the neighborhood of the air potential core's tip. The exponent in the initial region is $-5/3$ and in the final region is $-7/3$, values which lie slightly below and above the value 2. Recent experimental evidence[3], taken by probe at conditions corresponding to the initial region, also lend support to the value $-5/3$. (The value reported by Chriss is -1.7.)

Having determined particle size (hence K_s) and N(0, z), it is possible to equate $K_\lambda(r)/K_\lambda(0)$ with $N(r)/N(0)$. The $K_\lambda(r)$ profiles, obtained by Abel inversion, are shown for six axial stations in Fig. 12. The radial coordinate has been nondimensionalized with respect to K_λ's half-radius, r_K. It is seen that the two profiles measured in the initial region are quite closely gaussian whereas those taken further downstream depart from the gaussian curve at large radii.

Knowing particle density as a function of r and the global mass flow rate allows the determination of the average cross-sectional particle velocity $\langle u \rangle_w$. This quantity is shown in Fig. 13. In the final region, it is seen that $\langle u \rangle_w \sim z^{-1}$ as in the subsonic case. Although there are not sufficient points taken in the initial region to determine the slope of $\langle u \rangle_w$, consistency with r_1, r_2, and N(0) requires that $\langle u \rangle_w \sim z^{-1/3}$ in this region. This variation does not violate the concept of a potential core if it is borne in mind that $\langle u \rangle_w$ encompasses velocities both within and outside of the potential core. Also shown in the figure is the centerline air velocity obtained by a direct pitot probe measurement without water injection. For the sake of more direct, comparison, the cross-sectional average air velocity was computed from probe measurements by the expression

$$\langle u \rangle_a = \frac{\int_0^\infty \rho u r\, dr}{\int_0^\infty \rho r\, dr} \qquad (25)$$

It is seen that this velocity curve fairs smoothly into the $\langle u \rangle_w$ curve in the final region but lies above $\langle u \rangle_w$ in the initial region. One might be prompted to equate this difference with a slip velocity were it not for the fact that particles of this size, based on calculations using the most conservative (Stokes) drag coefficient, should be fully accommodated by the time they reach the first measurement station. A more probable explanation is that initially the water inertia exerts alocal retardation on the air stream but that, as mixing progresses, the overwhelming air/fuel momentum ratio makes itself felt with the result that little difference exists in the downstream air velocity with or without injection. In this regard, the water particles might be considered as a passive contaminant.

The axial variations of several quantities measured in this test series are summarized in Table 2. In considering the table, the variations ascribed to the final, fully developed, zone are to be regarded as the most reliable as more data points exist in this zone, In all cases, exponents have been estimated to the nearest fraction.

V. Summary and Conclusions

Results of a non-interfering light scattering experiment applied to supersonic mixing of water with air have been presented. Power law behavior has been noted for centerline density and spreadtng rates in two distinct regions. These regions correspond to the outer air jet's virtual potential core and subsequent fully developed region. The water density profile in the potential region is gaussian.

	Initial Zone	Final Zone
$K_\lambda(0)$	$z^{-5/3}$	$z^{-7/3}$
$\int_0^\infty K_\lambda \, dr$	$z^{-2/3}$	$z^{-2/3}$
$\int_0^\infty K_\lambda \, r \, dr$	$z^{1/3}$	z^{1}
r_1	z^{1}	$z^{5/3}$
r_2	z^{1}	$z^{5/3}$
$N(0)$	$z^{-5/3}$	$z^{-7/3}$
$\langle u \rangle_w$	$z^{-1/3}$	z^{-1}

Table 2. Axial Variation of Axisymmetric Jet Mixing Parameters

It has been shown that a monodisperse light scattering analysis is applicable to particle flows generated by large initial velocity difference. Graphical techniques have been used to obtain, without Abel inversion, centerline density and characteristic mixing radii. These techniques are applicable, after suitable change of variable, to all lineintegrated measurements taken of a cylindrically symmetric medium.

Acknowledgments

This work was supported by the Air Force Aero Propulsion Laboratory, Wright-Patterson Air Force Base, Ohio, under Contract No. F33615-67-C-1122. The author also wishes to express his appreciation to Professor J. A. Nicholls who initiated and encouraged this research.

Nomenclature

a_λ	fractional attenuation due to scattering
D	particle diameter
D_{32}	$\overline{D^3}/\overline{D^2}$ particle volume/surface ratio
K_λ	scattering extinction coefficient
K_s	scattering-area coefficient
I_λ	spectral radiance
L	optical path length
ℓ	optical path variable
M	Mach number
$\dot{m}$	mass flow rate
N	particle number density
R	inner jet radius
r	radial coordinate
r_o	outer jet exit radius
u	velocity
y	transverse coordinate
z	axial coordinate
α	scattering parameter, $\pi D/\lambda$
λ	wavelength
ρ	mass density

Subscripts

a	air
w	water, inner jet

Averages

$\overline{(\ )}$	particle average
$\overline{\overline{(\ )}}$	particle area average
$\langle\ \rangle$	jet cross-sectional average

References

1. Schetz, J.A., "Analysis of the Mixing and Combustion of Gaseous and Particle-Laden Jets in an Air Stream," AIAA 7th Aerospace Sciences Meeting, New York, January 20-22, 1969.

2. Zakkay, V., Krause, E., and Woo, S.D.L., "Turbulent Transport Properties for Axisymmetric Heterogeneous Mixing," AIM J., 2, 11, November 1964.

3. Chriss, D.E., "Experimental Study of the Turbulent Mixing of Subsonic Axisymmetric Gas Streams," AEDC TR 133, Arnold Air Force Ration, Tennessee, August 1966 (AD672975).

4. Kling, R., "La Formation et L'Evolution des Brouillards Combustibles," Agardograph 9, Combustion Researches and Reviews, Butterworths Publications, London, 1955.

5. Dobbins, R.A., "Measurement of Mean Particle Size in a Gas-Pastide Flow," AIAA J., 1, 1940, 1963,

6. Dobbins, R.A. and Strand, L.D., "A Comparison of Two Methods of Measuring Particle Size of Al_2O_3 Produced by a Small Rocket Motor," AIAA Paper No. 69-146, Seventh Aerospace Sciences Meeting, New York, January 1969.

7. Crowe, C.T. and Willoughby, P.G., "A Mechanism for Particle Growth in a Rocket Nozzle," AIAA J., 4, 9, 1677-1678, 1966.

8. Mugele, R.A. and Evans, H.D., "Droplet Size Distribution in Sprays," Ind. and Eng. Chem., 43, 1317-1324, 1951.

9. Dobbins, R.A., "Applications of Light Scattering in Research and Technology," 6th AIM Aerospace Sciences Meeting, New York, January 1968.

10. Houghton, H.G. and Chalker, W.R., "The Scattering Cross-section of Water Drops in Air for Visible Light," J.O.S.A., 39, 11, 995-957, 1949.

11. Dobbins, R.A. and Jizmagian, S.G., "Optical Scattering Cross Sections for Polydispersions of Dielectric Spheree," J.O.S.A., 56, 10, 1345-1350, 1966.

12. Bracewell, R., The Fourier Transform and its Applications, McGraw-Hill. New York, 1965.

13. Nestor, O.H. and Olsen, N.H., "Numerical Methods for Reducing Line and Surface Probe Data," SIAM Rev., 2, 3, July 1960.

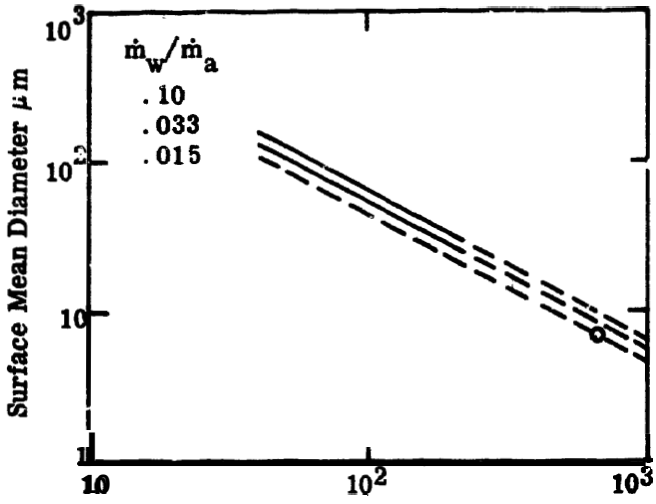

Figure 1. Particle Size vs. Velocity (extrapolated from Ref. 4)

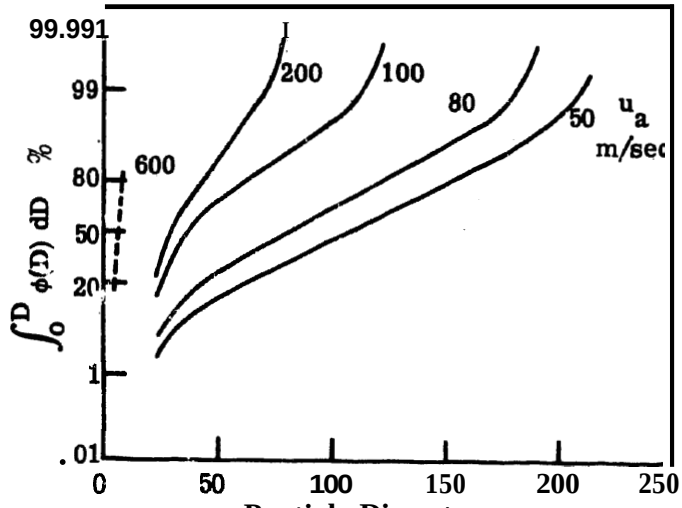

Figure 2. Cumulative Drop *Size* Distribution vs. Relative Velocity

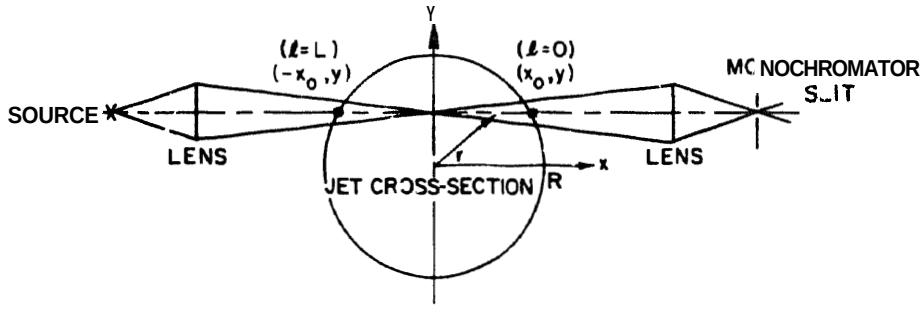

Figure 3. Optical Schematic

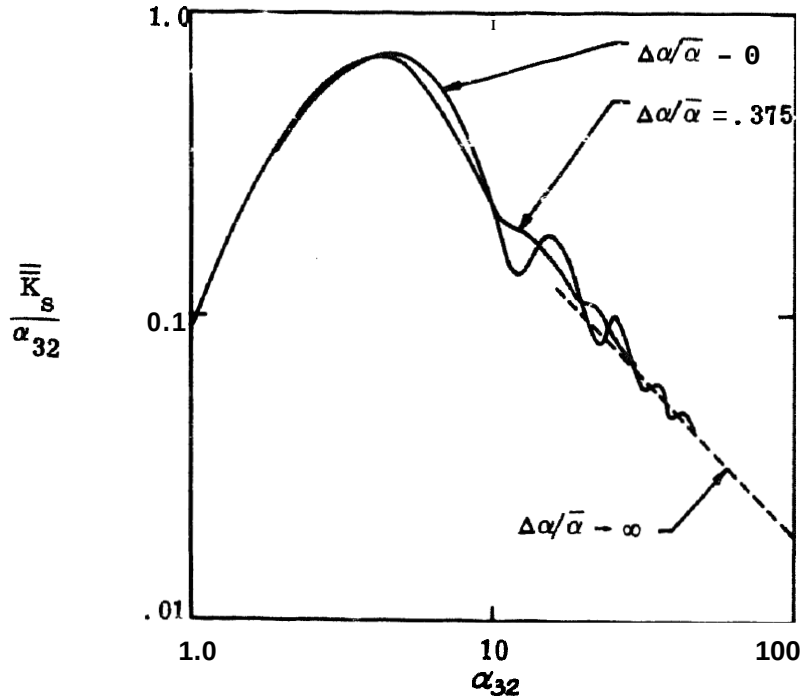

Figure 4. Specific Scattering-Area Coefficient

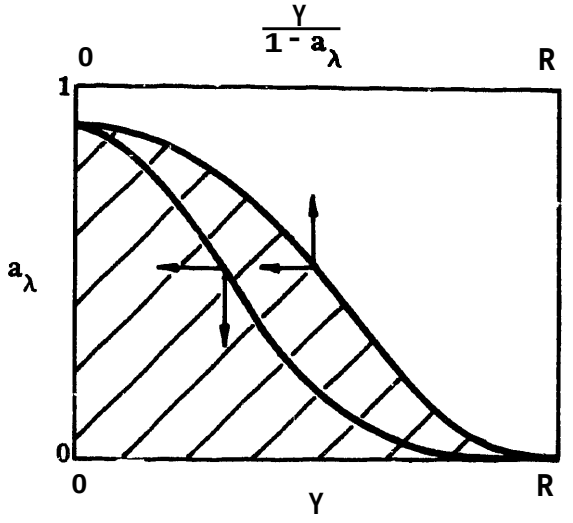

Figure 5. Graphical Determination of $\pi \int_0^R K_\lambda(r)\, r\, dr$

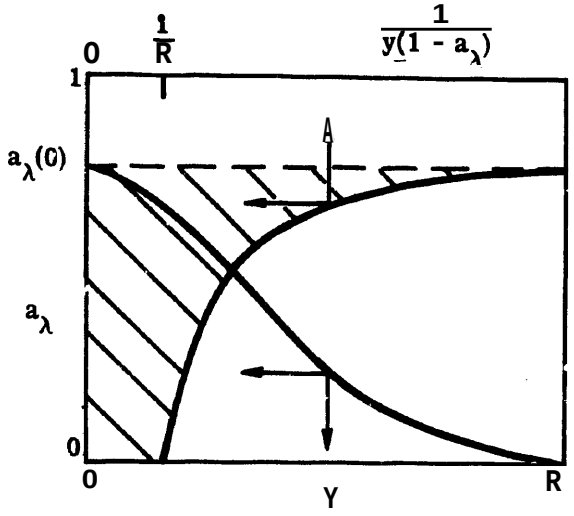

Figure 6. Graphical Determination of $K_\lambda(0)$

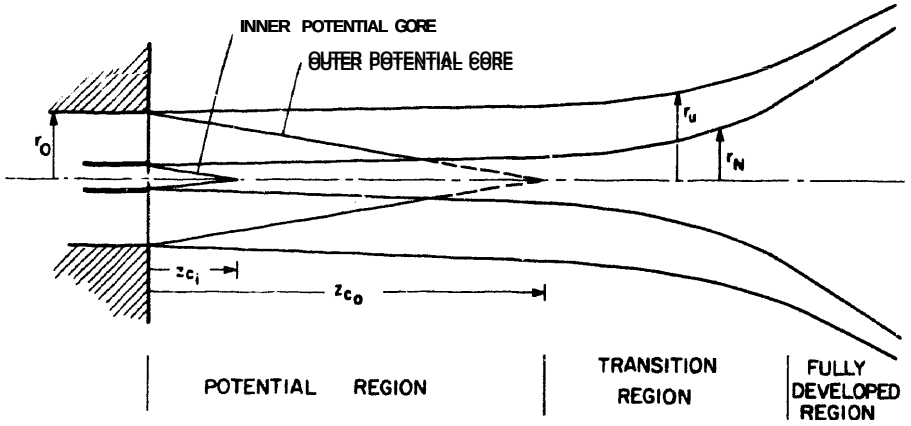

Figure 7. Supersonic Coaxial Jet Mixing Configuration

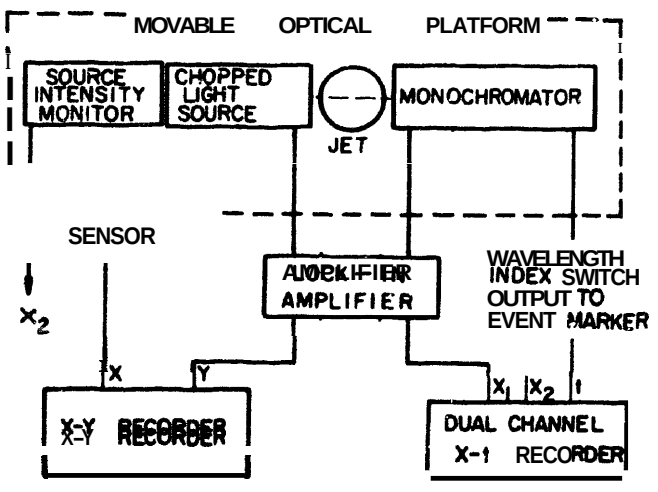

Figure 8. Instrumentation

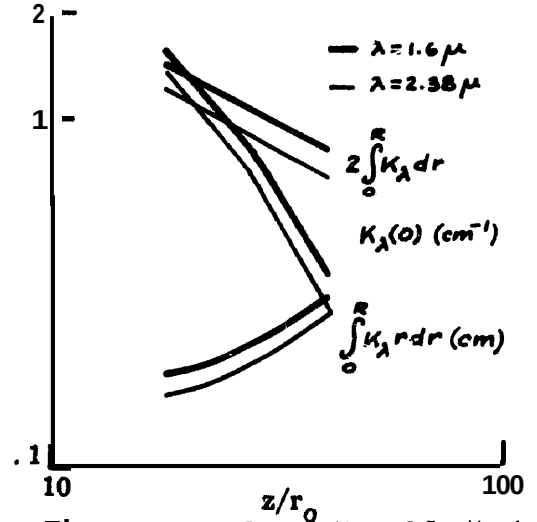

Figure 9. Axial Variation of Scattering Coefficient — Centerline Value, Path Integral, and Cross-Section Integral. ($\bar{\rho}$ = 0.44, r_0 = .893 cm)

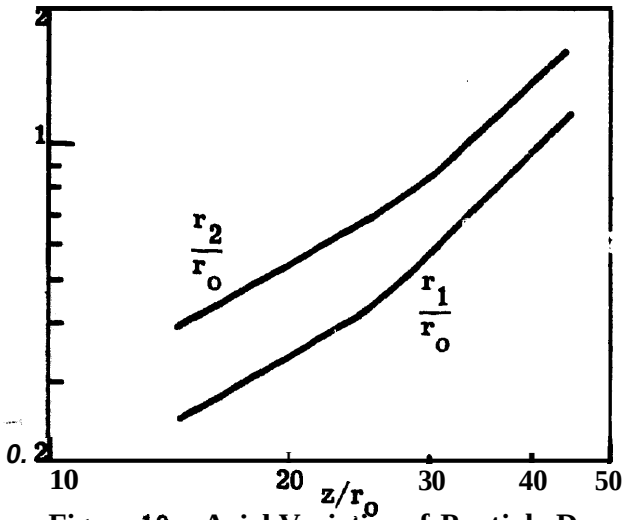

Figure 10. Axial Variation of Particle Density Integral Radii
($\rho u_w/\rho u_a = 0.44$, $r_o = 0.893$ cm)

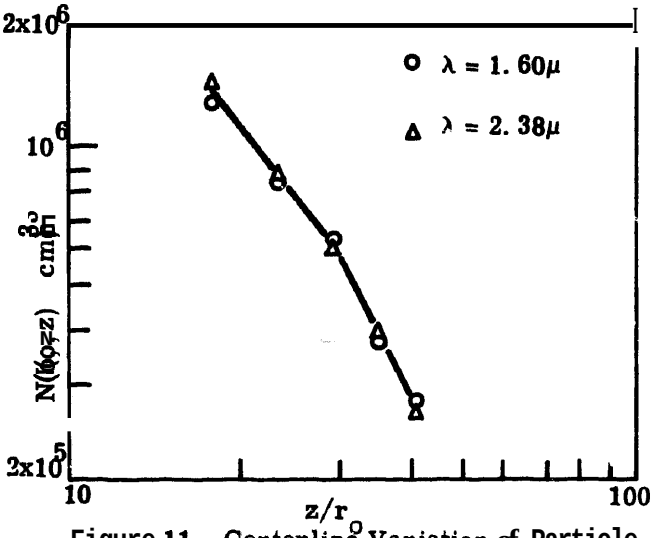

Figure 11. Centerline Variation of Particle Number Density
($\rho u_w/\rho u_a = 0.44$, $r_o = 0.893$ cm)

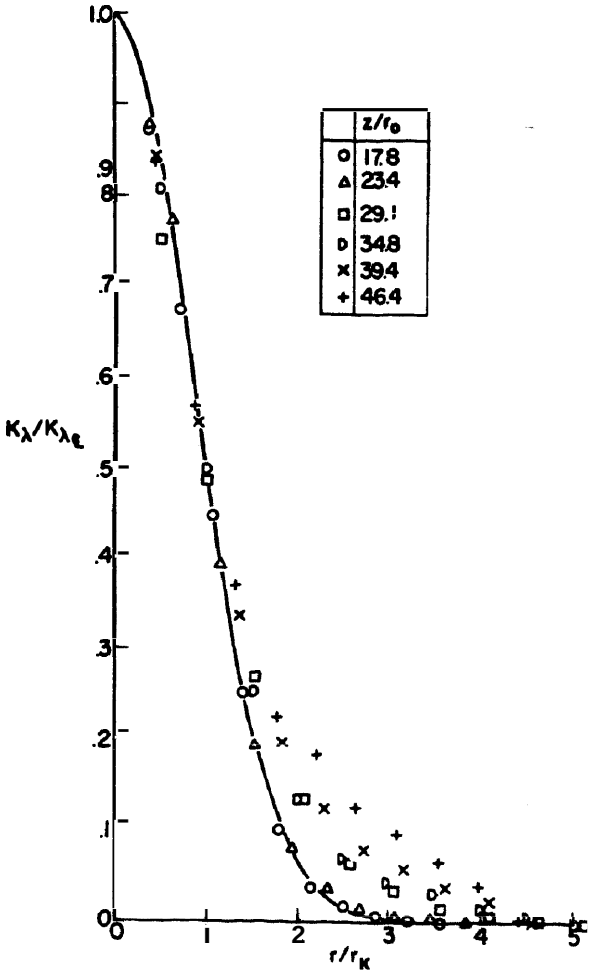

Figure 12. Abel-inverted Extinction Coefficient Normalized to Centerline Value and Half-Radius

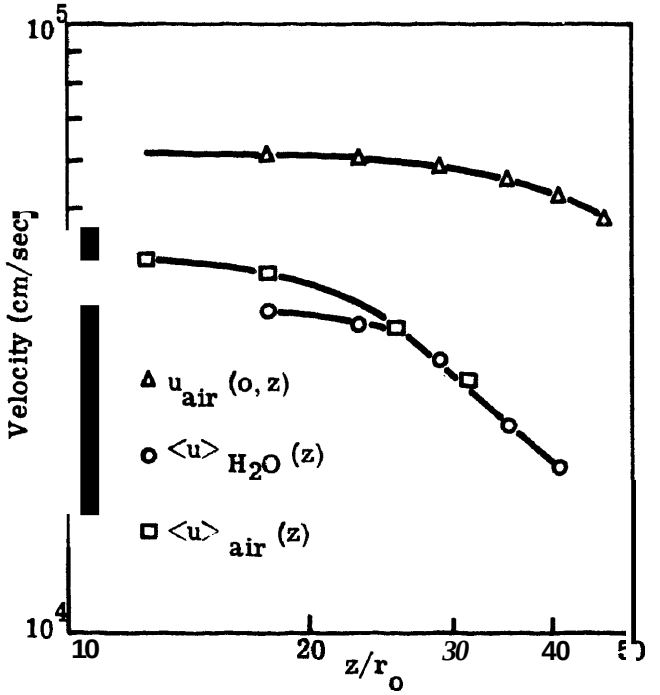

Figure 13. Centerline and Average Air Jet Velocity (without Water Injection) and Average Water Velocity vs. Distance from Injection Plane ($\rho u_w/\rho u_a = 0.44$, $r_o = .893$ cm)